Simultaneous and coordinated rotational switching of all molecular rotors in a network

Y. Zhang, H. Kersell, R. Stefak, J. Echeverria, V. Iancu, U.G.E. Perera, Y. Li, A. Deshpande, K.-F. Braun, Christian Joachim, et al.

Simultaneous and Coordinated Rotational Switching of All Molecular Rotors in a Network

Y. Zhang[1], H. Kersell[1], R. Stefak[2], J. Echeverria[2], V. Iancu[1], U. G. E. Perera[1], Y. Li[1], A. Deshpande[1], K.-F. Braun[1], C. Joachim[2], G. Rapenne[2,3], & S.-W. Hla[1,4,]*

[1]Nanoscale & Quantum Phenomena Institute, Physics & Astronomy Department, Ohio University, Athens, OH 45701, USA.
[2]CEMES, CNRS, 29 rue J. Marvig, 31055 Toulouse, France.
[3]Universite´ de Toulouse, UPS, 118 route de Narbonne, 31062 Toulouse, France.
[4]Center for Nanoscale Materials, Nanoscience and Technology Division, Argonne National Laboratory, IL 60439, USA.
Corresponding author: hla@ohio.edu*

A range of artificial molecular systems have been created that can exhibit controlled linear and rotational motion. In the development of such systems, a key step is the addition of communication between molecules in a network. Here, we show that a two-dimensional array of dipolar molecular rotors can undergo simultaneous rotational switching by applying an electric field from the tip of a scanning tunnelling microscope. Several hundred rotors made from porphyrin-based double-decker complexes can be simultaneously rotated when in a hexagonal rotor network on a Cu(111) surface by applying biases above ±1 V at 80 K. The phenomenon is observed only in a hexagonal rotor network due to the degeneracy of the ground state dipole rotational energy barrier of the system. Defects are essential to increase electric torque on the rotor network and to stabilize the switched rotor domains. At low biases and low initial rotator angles, slight reorientations of individual rotors can occur resulting in the rotator arms pointing in different directions. Analysis reveals that the rotator arm directions here are not random, but are coordinated to minimize energy via cross talk among the rotors through dipolar interactions.

Molecular machines are ubiquitous in nature and are the backbone of many vital biological processes[1-5]. Most natural molecular machines are sensitive to their environment, but lack adaptability to new media and functions. In contrast, artificial molecules that mimic some machine functions[6-9] can be engineered to suit more specific environments than natural molecular machines, and are thus advantageous in the development of solid-state devices. In recent years, complex molecular systems have been created on solid surfaces that can undergo directed linear motion[8] or controlled rotation motion[7,9]. In particular, double- and multi-decker complexes have been fabricated that can be considered analogues of rotational devices[10-19]. These species can be vacuum deposited intact on metal surfaces[12,16-19] using source temperatures as high as 800 K[16], and are therefore well-suited for study in atomically clean environments.

The molecular rotors used here are donor-acceptor-porphyrinate naphthalocyaninate europium double-decker complexes[20] (Fig. 1a). The upper deck is a functionalized 5,15-diarylporphyrin, which is designed to act as a rotator. It has a permanent electric dipole moment of 8 Debye due to the presence of an electron donating and an electron accepting group (butoxy and cyano groups, respectively) located at the opposite positions on the porphyrin macrocycle (Fig. 1a). The lower deck, stator, is a naphthalocyanine designed to anchor on metallic surfaces via 8 sulfur atoms at the end of the macrocycle (Fig. 1a). The upper and lower decks are linked *via* a europium(III) ion, which acts as an atomic ball bearing. Although self-assembled networks of double-decker molecular rotors have been already demonstrated on surfaces[10-15,18], their synchronized rotations have yet to be realized. Scanning tunneling microscope (STM) is a unique instrument to demonstrate operation of molecular machines on surfaces using a variety of manipulation schemes [8,9,15,17,21-24].

We explore the structure of molecular rotors on single crystal surfaces of Au(111) and Cu(111). For a similar deposition time on substrates held at room substrate temperature, individual rotors are observed on Au(111) while ordered self-assembled structures with a hexagonal symmetry of rotors are formed on Cu(111) (Fig. 1c, and supplementary information S1). Interestingly, the individual rotors on Au(111) are rotating even at 5 K and thus they appear circular (Fig. 1b) in STM images[9,21,24] confirming that the rotator arm with added donor and acceptor units rotates as designed. The rotation here is driven by thermal energy and it should be a random back-and-forth motion. Unlike our previous study of a standalone molecular motor on Au(111)[9], where the rotation can be terminated at reduced surface temperature of 5 K, the observed rotation at this temperature indicates a low rotational barrier. In agreement with this, the calculated rotational barrier for the individual rotor on the surface is found to be ~ 5meV. On Cu(111), however, the rotors in networks appear stationary up to 80 K. Since the molecule-surface interaction is rather weak (supplementary information S2), such static position should be due to interactions with neighbouring molecules including non-polar interactions in the network. In STM images, the rotator arm of each stationary rotor in the network appears as two protruding lobes. The calculated STM image of a rotor on the surface also shows the exact same appearance with two pronounced protrusions originated from the upward tilted π-rings caused by internal steric effects (Fig. 1d and 1e). Here, the protrusion of the acceptor is more pronounced than the donor in the rotator arm. The STM image calculations are performed by using the Elastic Scatterring Quantum Chemistry approach, which is the most direct way to compare with the experimental STM image because it calculates a complete scattering process occurring at the junction including not only the molecule and the surface, but also the tip apex, the tip body, the surface supporting sample and the bias as well. For the electronic structure of the molecule, however, the density functional theory calculations can give more precise results, which we have performed only for the isolated molecules due to the limitations in computation space (see method section and supplementary information).

Simultaneous rotation

During STM imaging of the hexagonal network of rotors on Cu(111) the orientation of the rotator arms can be switched when biases higher than ±1 V are used (Fig. 2a). Amazingly, all the rotators within the scanning range can be simultaneously realigned to a new direction after switching, and the entire network within the tip scanning area is now pointing to a new direction (Fig. 2a). As a consequence, the domain boundaries between the regions having different rotator alignments are formed, which can be observed in large area STM images. Figures 2b and 2c present two subsequent STM images of the exact same surface area where the rotators from some regions in the first image have been switched to new orientations thereby creating local domains.

Rotational switching in the hexagonal network here can be, indeed, purposely induced using the STM tip. A typical sequence is presented in figure 2d to 2f. For the tip-induced switching, the STM tip is positioned above the rotor network shown in Fig. 2d, and then the bias is ramped from 0 to 1.25 V. The recorded tunneling current during this process increases as the bias is raised until a sudden drop in the current occurs at ~0.93 V (Fig. 2e). The subsequent STM image (Fig. 2f) shows that the entire network within the image frame has been rotated clockwise by 70° from the original direction. This procedure can be repeatedly performed but rotational angle varies. From such measurements, we determine that the threshold energy of ~1.0±0.3 eV is required to induce the rotations in the network. Statistical analysis on the rotational switching of 5176 rotors reveals an equal probability of switching to the clockwise and anticlockwise directions within the measurement uncertainty of ±5%. Fig. 2g presents a pi-chart for the measured switching angles, which are binned for ±5°. In both directions, switching occurs to all the angles up to 70°. The higher the rotated angle the larger the energy at the domain boundary and this might be the limiting factor for the observed maximum angle. Such rotational

switching of rotators can be induced with both positive and negative bias polarities (Fig. 2h). In order to check the observed phenomenon further, a parallel network of rotors is formed (supplemental information). However, attempts to induce rotation in the parallel rotor network were not successful: The rotators remained stationary until they were destroyed at high biases above 2.3 V.

Rotation mechanism

To understand the observed synchronized rotation mechanism the total energy of the rotor network[25-27] is analyzed, which can be described as:

$$E = \{KE_{rot} + U_{dipl} + U_{el} + U_{str} + U_T\} \_\_\_\_\_ (1)$$

where, 'KE_{rot}' is the internal rotational kinetic energy, 'U_{dipl}' is the dipolar energy, 'U_{el}' is the electric field energy[28], 'U_{str}' is the structural energy including the dispersion interactions in the network, and 'U_T' is the thermal energy corresponding to 80 K substrate temperature, respectively. This can be expanded to

$$E = \left\{\frac{\hbar^2}{2I}J(J+1)\right\} + \left\{\frac{1}{4\pi\epsilon}\left[\sum_j\left(\frac{\vec{\mu}.\vec{\mu_j}}{r^3} - \frac{3(\vec{\mu}.\vec{r}).(\vec{\mu}_j.\vec{r})}{r^5}\right)\right]\right\} + \left\{\left[\frac{V_t}{d}\frac{(s+s^2)^{1/2}s_z}{\log[s^{1/2}+(1+s)^{1/2}]}\right]cos\delta.\mu.cos\gamma\right\} + U_{str} + U_T \_\_\_\_(2)$$

Here, the first term belongs to the internal rotational kinetic energy of rotors; 'I' is the moment of inertia and 'J' is the rotational quantum number. The calculated moment of inertia is 5.52 x 10^{-44} kg m^2, which gives a very small internal rotational kinetic energy in the order of tens of μeV. Thus, a significant contribution of KE_{rot} can be ignored. In equation (1), U_{el} and U_T supply the energy for the rotations while U_{dipl} and U_{str} act as the energy barrier. Since the rotation of the network can be induced at 80 K by adding additional electric field from the STM tip, the components of U_T and U_{el} provide a sufficient energy to overcome the rotational barrier.

In STM images, the donor and acceptor of the rotator appear with a slight height difference (Fig. 3a, and supplementary information) as in the calculated image (Fig. 1d). From the image, we can assign the

dipole direction to be pointing towards the donor, i.e. to the less protruding part of the rotator arm. All the rotator arms in the network appear unidirectional (Fig. 3a) implying that all the dipoles are pointing to the same direction, and hence it is a ferroelectric system. Such 2-D ferroelectric system formed by molecular rotors may have potential applications [30].

In the dipolar energy term, $U_{dipl,}$ described in the second term in the equation (2)[25,29], '$\vec{\mu}$' and '$\vec{\mu_j}$' are the dipole vectors of the central and the neighbouring rotators, '$\vec{r}$' is the distance vector, and 'ε' is the dielectric constant (Fig. 3a, and 3b). The dipolar energy of the network is calculated by considering up to 8th neighbor rotators (supplementary information). Let us first consider a scenario where a single rotor is rotating while all other rotors are at rest (Fig. 3b). As soon as the rotor starts to turn from its initial position, the symmetry of the dipole orientation in the hexagonal network will be broken. Conceivably, it will experience a varying force exerted by the neighbouring dipoles. The calculated dipolar energy barrier of the hexagonal network increases as the central rotator starts rotating and it maximizes at the 180° turn (Fig. 3c). Thus, 360° rotation of a single rotator in the network is not favorable.

Strikingly, when all the rotators are rotated simultaneously in a synchronized manner, an entirely different energetic landscape occurs (Fig. 3c). The dipolar energy barrier for rotation of the hexagonal network remains constant, i.e. $\Delta E = 0$, and thus it appears as a straight line. Thus synchronized rotation is the most favorable condition. Further analyses on the synchronized rotation in a parallel network as well as random rotation sequences show that only the synchronized rotation in the hexagonal network produces such an effect (supplementary information). Using the Luttinger and Tisza scheme, Brankov and Denchev[31] have proposed that the ground state of an infinite hexagonal dipole network is degenerate, and that such system should be ferroelectric. Although it is based on a simple dipole network model, their proposal is very well in agreement with our findings. To date, only light induced

collective switching via isomerization of molecules[32] has been demonstrated. The collective switching here is induced by dipolar interactions in a ferroelectric network of molecular rotors.

Next, the energy supplied by the STM tip, U_{el}, is estimated by using a spherical charge model[28] described in the third term of equation (2) with the tip radius of 'R = 3 nm', as well as a point charge model. In the former case, 'V_t' is the tunneling bias, 'd' and 'z' are the tip-rotor, and tip-surface distances, 's = d/R', and s_z = z/R, while 'δ' and 'γ' are the angles between the electric field and the rotating plane, and the rotor directions, respectively (supplementary information). Both models give a similar maximum energy (Fig.3d) ranging from ~50 meV to over 300 meV for various biases from 0.4 V to 2.4 V at 0.5 nm tip height.

Roles of defects

To induce rotation, there must be an external net torque exerted on the rotators. The electric field emanating from the STM tip simultaneously acts on many rotators in the network (Fig. 4a), and for a perfect hexagonal network of rotors, a clockwise electric torque 'τ' experienced by any rotator has its anticlockwise counterpart '$-\tau$' at the opposite symmetric site. Thus, the torques are cancelled out and, there is no net electric torque on the system; $\tau_{net} = 0$. Interestingly, when a defect is formed by a missing rotor or a miss-aligned rotator arm, then a net electric torque having the exact magnitude of the missing one appears at the opposite symmetric location since it is no longer cancelled. This results in a large net torque gain in the network. On the other hand, formation of the defect breaks the network symmetry, and consequently the dipolar energy increases at the defect site, which then acts as a barrier to maintain rotor domains. Thus, the defects act dual roles; to increase the net torque for switching while at the same time, to pin the switched domains. This invokes further questions on how these two factors

balance. The torques exerted on the rotators can be estimated by using the relationship, $\tau = \mu\varepsilon\, cos\delta\, sin\gamma$, where '$\varepsilon$ ' is determined by using the spherical charge model described above (Fig. 4b). Figure 4c presents a calculated net torque for a tip radius of 3 nm and the dipolar energy generated by a single defect. Because of the $1/r^3$ dependence, the dipole barrier rapidly decays with the distance while the net torque attenuates at a much slower pace with less than 1/r dependence of the electric field to the distance. As a result the third or higher order neighbouring rotators from the defect site experience only a negligible amount increase or no change in dipolar energy barrier while they gain a net electric torque thereby enabling rotation. Thus, the defects are essential for the observed rotational switching mechanism. This is exactly reflected in the experiments where rotational switching domains are observed only at the vicinity of the defects as evident in Fig. 2. Note that the sizes of the tip-apex in our experiments are much smaller than most conventional STM tips because we use a local tip-preparation procedure and calculations show that increasing the tip radius to 50 nm still maintain similar trend (supplementary information). For the defective areas, switching probability exceeds to 67.2% and the switched domain sizes vary from a single rotor chains to over 500-rotor-wide regions depending on the locations and the number of defects (supplementary information). The domains are mostly observed away from the step-edges. This is because the rotors at the step-edges are not surrounded by a complete hexagonal network, and consequently, the rotation is not favorable at step-edges.

Since a large number of rotors in the network simultaneously experience the electric field of the tip, we have not achieved directed rotation selectively controlled by the STM tip. Because of the 'sin γ' dependence of the electric torque, where the 'γ' is the angle between the electric field direction and the dipole orientation (Fig. 4b), the net electric torque increases with increasing initial rotator angle to the electric field direction and it maximizes at 90° (Fig. 4d). Accordingly, the maximum switching angle also increases with the increasing initial rotator angle to the tip position.

Coordinated rotation

Below the threshold bias, the electric field strength may not be sufficient to drive a synchronized rotation. However, slight reorientations of the rotator arms can still occur. Here, the rotator arms are oriented to different directions within 4 to 15 degrees from their initial unidirectional alignment (Fig. 4e). This effect is also induced by electric field of the STM tip, and defects are necessary to generate and maintain such rotator orientations. By increasing the bias the number of reoriented rotator arms increases (Fig. 4f). Amazingly, although their orientations appear random at a first glance in Fig. 4e, a careful analysis reveals that the directions of the rotator arms here are well coordinated to minimize the energy. To demonstrate this, the dipolar energy of six rotator arms labeled as 1 to 6 in Fig. 4e are calculated by reorienting the neighboring rotator arms from their initial position, i.e. 90 degree to a hexagonal axis, to the current directions (Fig. 4g). Because of $1/r^3$ dependence of the dipolar energy, six consecutive hexagons representing the first near neighbor dipoles, which are the most influential, are sufficient to find their energetic landscapes. When one or more rotators are rotated from the initial angle to their measured angle, the net dipolar energy of the hexagon fluctuates above or below an equilibrium value (Fig. 4g). Only when all the rotators are rotated at their measured angles within each hexagon, the net dipolar energy becomes closer to the equilibrium within ± 0.4 meV. Thus the rotators within each hexagon reorient either clockwise or anticlockwise directions to achieve a minimum energy configuration as if they are connected by a string. This clearly indicates a cross talk among the rotors and the rotator reorientations here are not random but are well coordinated[27].

Conclusions

In summary, we have demonstrated simultaneous and coordinated rotation of molecular rotors by introducing dipoles into a hexagonal rotor network. Theoretical analyses reveal that synchronized

rotation is the most favorable condition for simultaneous rotations due to degeneracy of the ground state dipole rotational potential barrier. Moreover, defects are the key for the observed rotations and domain formations. These findings represent the first direct visualization of dipole interactions in a hexagonal network manifesting mesoscale behaviours collectively achieved by individual rotors. With this achievement, the possibility to operate billions of molecular machines packed in a tiny surface area for potential applications in solid state devices, quantum computation, energy transfer, and information transport at the nanoscale is a step closer.

Methods: The STM experiments were performed by using a custom-built ultra-high-vacuum low-temperature STM system[33] operated at a base pressure below 4 x 10^{-11} Torr. An electrochemically etched polycrystalline tungsten wire was used as the STM tip. Single crystal Au(111), and Cu(111) samples were cleaned by repeated cycles of neon ion sputtering and annealing. The molecules were deposited on atomically cleaned samples held at room temperatures by thermal evaporation using a custom-built Knudsen cell in an ultrahigh vacuum environment. The molecular source temperature for the deposition was 60°C (333 K). The samples were then transferred to the STM chamber in-situ. Subsequently the sample temperature was lowered to 80 K or 5 K for separate experiments. The density functional theory (DFT) calculations of the molecular structure without including the surface were performed by using CRENBL ECP basis[34] for the Europium atom and a 6-31G Basis for the rest of the molecular components, respectively. The dipole moment and the moment of inertia for the rotor were calculated on converged rotor structure from DFT calculations. The constant current STM images were calculated using the Elastic Scatterring Quantum Chemistry (ESQC) theory[35]. In ESQC, starting from the complete mono-electronic Hamiltonian of the STM junction, an effective Hamiltonian technique was used to calculate the exact multichannel scattering matrix of the tip-molecule-sample junction. Then, the generalized Buttiker-Landaueur formula was used to calculate the tunnel current intensity through

the molecule for a given tip-surface distance. A constant current image was achieved after optimizing the tip distance at each calculated image point. This numerical feedback loop was integrated in the ESQC STM image calculations. In the junction, the rotor adsorbed on the Au(111) surface was described by using a complete *s*, *p* and *d* basis set for the Eu atoms, and the 4*f* electrons were included in the electronic core. C, N, O and S atoms were described by a *s,p* basis set and H by its 1*s* orbital. Before each image calculation, the geometry of each molecule was optimized by using the ASED+ semi-empirical molecular mechanics routine[36] with the same Slater atomic orbital basis set as the one used for ESQC.

References

1. Browne, W.R., & Feringa, B.L. Making molecular machines work. *Nature Nanotech.* **1**, 25-35 (2006).

2. Bath, J., & Turberfield, A.J. DNA nanomachines. *Nature Nanotech.* **2**, 275-284 (2007).

3. Carter, N.J., & Cross, R.A. Mechanics of the kinesin step. *Nature* **435**, 308-312 (2005).

4. Goel, A., & Vogel, V. Harnessing biological motors to engineer systems for nanoscale transport and assembly. *Nature Nanotech.* **8**, 465-475 (2008).

5. Uchihashi, T., Iino, R., Ando, T., & Noji, H. High-speed atomic force microscopy reveals rotary catalysis of rotorless F_1-ATPase. *Science* **333**, 755-758 (2011).

6. Finnigan, G.C., Hanson-Smith, V., Stevens, T.H. & Thornton, J.W. Evolution of increased complexity in a molecular machine. *Nature* **481**, 360-365 (2013).

7. van Delden. R.A. et al. Unidirectional molecular motor on a gold surface. *Nature* **437**, 1337-1340 (2005).

8. Kudernac, T. et al. Electrically driven directional motion of a four-wheeled molecule on a metal surface. *Nature* **479**, 208-211 (2011).

9. Perera, U.G.E. et al. Controlled clockwise and anticlockwise rotational switching of a molecular motor. *Nature Nanotech.* **8**, 46-51 (2013).

10. Ye, T., Takami, T., Wang, R., Jiang, J., & Weiss, P.S. Tuning interactions between ligands in self-assembled double-decker phthalocyanine arrays. *J. Am. Chem. Soc.* **128**, 10984-10985 (2006).

11. Takami, T. et al. Controlled adsorption orientation for double-decker complexes. *J. Phys. Chem. C*. **111**, 2077-2080 (2007).

12. Komeda, T. et al. Observation and electric current control of a local spin in a single-molecule magnet. *Nature Comm.* **2**, 217 (2011).

13. Otsuki, J., Komatsu, Y., Kobayashi D., Asakawa, M., & Miyake, K. Rotational liberation of a double-decker porphyrin visualized. *J. Am. Chem. Soc.* **132**, 6870–6871 (2010).

14. Tanaka, H. et al. Molecular rotation in self-assembled multidecker porphyrin complexes. *ACS Nano* **5**, 9575-9582 (2011).

15. Ecija, D. et al. Assembly and manipulation of rotatable cerium porphyrinato sandwich complexes on a surface. *Angew. Chem. Int. Ed.* **50**, 3872-3877 (2011).

16. Fahrendorf, S. et al. Accessing 4f-states in single-molecule spintronics. *Nature Comm.* **4**, 2425 (2013).

17. Fu, Y.-S. et al. Reversible chiral switching of bis(phthalocyaninato) terbium(III) on a metal surface. *Nano Lett.* **12**, 3931-3935 (2012).

18. Katoh, K. et al. Direct observation of Lanthanide(III)-Phthalocyanine molecules on Au(111) by using scanning tunneling microscopy and scanning tunneling spectroscopy and thin-film field-effect transistor properties of Tb(III)- and Dy(III)-Phthalocyanine molecules. *J. Am. Chem. Soc.* **131**, 9967-9976 (2009).

19. Isshiki, H. et al. Scanning tunneling microscopy investigation of tris(phthalocyaninato)yttrium triple-decker molecules deposited on Au(111). *J. Phys. Chem. C* **114,** 12202–12206 (2010).

20. Stefak, R., Ratel-Ramond, N., & Rapenne, G. Synthesis and electrochemical characteristics of a donor–acceptor porphyrinate rotor mounted on a naphthalocyaninato europium complex. *Inorg. Chim. Acta* **380**, 181-186(2012).

21. Gimzewski, J.K. et al. Rotation of a single molecule within a supramolecular bearing. *Science* **281**, 531–533 (1998).

22. Grill, L. et al. Rolling a single molecular wheel at the atomic scale. *Nature Nanotech.* **2**, 95-98 (2007).

23. Manzano, C. et al. Step-by-step rotation of a molecule-gear mounted on an atomic-scale axis. *Nature Mater.* **8**, 576-579 (2009).

24. Tierney, H.L. et al. Experimental demonstration of a single-molecule electric motor. *Nature Nanotech*. **6**, 625-629 (2011).

25. Kottas, G.S., Clarke, I.L., Horinek, & D., Michl, J. Artificial molecular rotors. *Chem. Rev.* **105**, 1281-1376 (2005).

26. Shih, Y.T., Liao, Y.Y., & Chuu, D.S. Rotational states of an adsorbed dipole molecule in an external electric field. *Phys. Rev. B.* **68**, 075402 (2003).

27. Mishima, K., & Yamashita, K. Quantum computing using rotational modes of two polar molecules. *Chem. Phys.* **361**, 106-117 (2009).

28. Devel, M., Girard, C., Joachim, C., & Martin, O.J.F. Field induced manipulation of fullerene molecules with the STM: a self-consistent theoretical study. *Appl. Surf. Sci.* **87**, 390-397 (1995).

29. Shima, H., & Nakayama, T. Dielectric anomaly in coupled rotor systems. *Phys. Rev. B.* **69**, 035202 (2004).

30. Akutagawa, T. et al. Ferroelectricity and polarity control in solid-state flip-flop supramolecular rotators. *Nature Mater.* **8**, 342-347 (2009).

31. Brankov, J.G. & Danchev, D.M. Ground state of an infinite two-dimensional system of dipoles on a lattice with arbitrary rhombicity angle. *Physica* 144A, 128-139 (1987).

32. Pace, G. et al. Cooperative light-induced molecular movements of highly ordered azobenzene self-assembled monolayers. *Proc. Nat. Acad. Sci.* **104**, 9937-9942 (2007).

33. Hla, S.-W. STM Single Atom/molecule manipulation and its application to nanoscience and technology. *J. Vac. Sci. Technol. B* **23**, 1351-1360 (2005).

34. Ross, R.B. et al. Ab initio relativistic effective potentials with spin-orbit operators .4. Cs through Rn. *J. Chem. Phys.* **93**, 6654-6670 (1990).

35. Sautet, P., & Joachim, C. Interpretation of STM images-copper-pathalocyanine on copper. *Surf. Sci.* **271**, 387-394 (1992).

36. Ample, F., & Joachim, C. A semi-empirical study of polyacene molecules adsorbed on a Cu(110) surface. *Surf. Sci.* **600**, 3243-3251 (2006).

Acknowledgements: This work (all the STM experiments as well as analytical and DFT calculations) is financially supported by the United State Department of Energy, Basic Energy Sciences grant no. DE-FG02-02ER46012. R.S., J.E., C.J. and G.R. acknowledge the support of the ANS P3N (AUTOMOL project n° ANR 09-NANO-040) for the chemical synthesis of molecules and STM image calculations. We thank ZYVEX for providing the molecules studied in the initial part of the project. S.W.H and K.F.B acknowledge the use of Ohio Supercomputing Centre (PHS0275).

Author contributions

S.W.H. conceived and designed the experiments: Y.Z., H.K., V.I, G.P., Y.L. and A.D performed the STM experiments; R.S. and G.R. synthesized the molecules; J.E. and C.J. performed STM image, adsorption site, and rotational barrier calculations; K.F.B, Y.Z and S.W.H performed the DFT and analytical calculations; Y.Z., H.K., V.I., and S.W.H analyzed the experimental data. All the authors discussed the results and commented on the manuscript.

Figure Legends

Figure 1. Structure and self-assembly of molecular rotors. **a**, A model of the rotor (top) and dipoles of rotator arms in a rotor array. The green and red colors indicate the opposite dipoles. **b**, STM image of rotating rotors on Au(111) surface at 5 K together with a zoom in STM image of a rotor [V_t = -1.5 V, I_t = 5.2 x10^{-11} A]. **c**, An STM image of self-assembled hexagonal rotor network on Cu(111) at 80 K [V_t = 1.1 V, I_t = 1.9x10^{-10} A]. A rotator arm is indicated with an oval. **d**, Calculated STM image of molecular rotor on surface revealing two asymmetric protrusions of the rotator arm. **e**, Rotor structure with vertically tilted π-rings indicated by two arrows. These π-rings produce the two-lobe contrast of rotors in STM images.

Figure 2. Simultaneous rotations. **a**, An STM image shows a sudden switching of rotators from green to blue arrow direction (~10° rotation) below a line indicated with an arrow [V_t = -2.3 V, I_t = 2 x 10^{-10} A]. **b**,

A large area STM image shows unidirectional alignment of rotator arms (labeled as A). **c**, The exact same area in a subsequent scan reveals the formation of different rotator domains (labeled as B and C) [V_t = 1 V, I_t = 3.2 x 10^{-10} A]. **d**, The tip is positioned above the blue dot in this STM image and voltage is ramped. **e**, The current rapidly decreases at ~0.93 V (indicated with an arrow). **f**, The subsequent image shows reoriented rotators [V_t = 0.7 V, I_t = 1.9 x 10^{-10} A]. The yellow ovals in **a, b**, **c, d** and **f** indicate defect sites. **g**, A pi-chart presents switching angles. The white line at the centre separates anticlockwise and clockwise rotations. **h**, Domain areas formed by rotation as a function of bias. Larger switched regions are observed when biases higher than ~± 1V (indicated by dashed lines).

Figure 3. Rotation mechanisms. **a**, STM image of a hexagonal rotor network ('0': a reference dipole and '1 – 6': nearest neighbours) showing color (height) contrast between the opposite rotator arms. **b**, A hexagonal dipole network model. **c**, Dipolar energy as a function of rotating angle for a single dipole rotation and synchronized rotation of all dipoles. **d**, The calculated electric field energies using a spherical tip (blue arrow) and a point charge model (red arrow).

Figure 4. Electric torque and coordinated reorientations. **a**, Electric field (blue arrows) of the tip (red dot) simultaneously acts on the rotors. When a defect (black oval) is formed, a net torque, '-τ', appears at the opposite site (red oval). **b**, The drawing illustrates the electric torque in 'xy' plane induced by the tip. **c**, The net torque (olive) decays slower than the dipolar energy barrier (red) from the defect site. **d**, The switching angles as a function of initial rotator alignment to the tip. Positive and negative 'γ' values are anticlockwise and clockwise rotation angles, respectively. The green curves are the torques. **e**, An STM image shows the rotator arms pointing to different directions [0.5 V, 1.8 x 10^{-10} A]. The angles are measured from a hexagonal axis as shown in the top-left corner. **f**, The percentage of reorienting

rotators increases with the increasing bias. **g** The net dipolar energy (red dots) of hexagon 1 to 6 in '**e**' changes after reorienting each rotator from 90°, and the green dots are the energies when all the rotators are reoriented to the measured angles. The dashed line marks the equilibrium energy of the hexagons and the gray box marks the region of ±0.4 meV from the equilibrium.

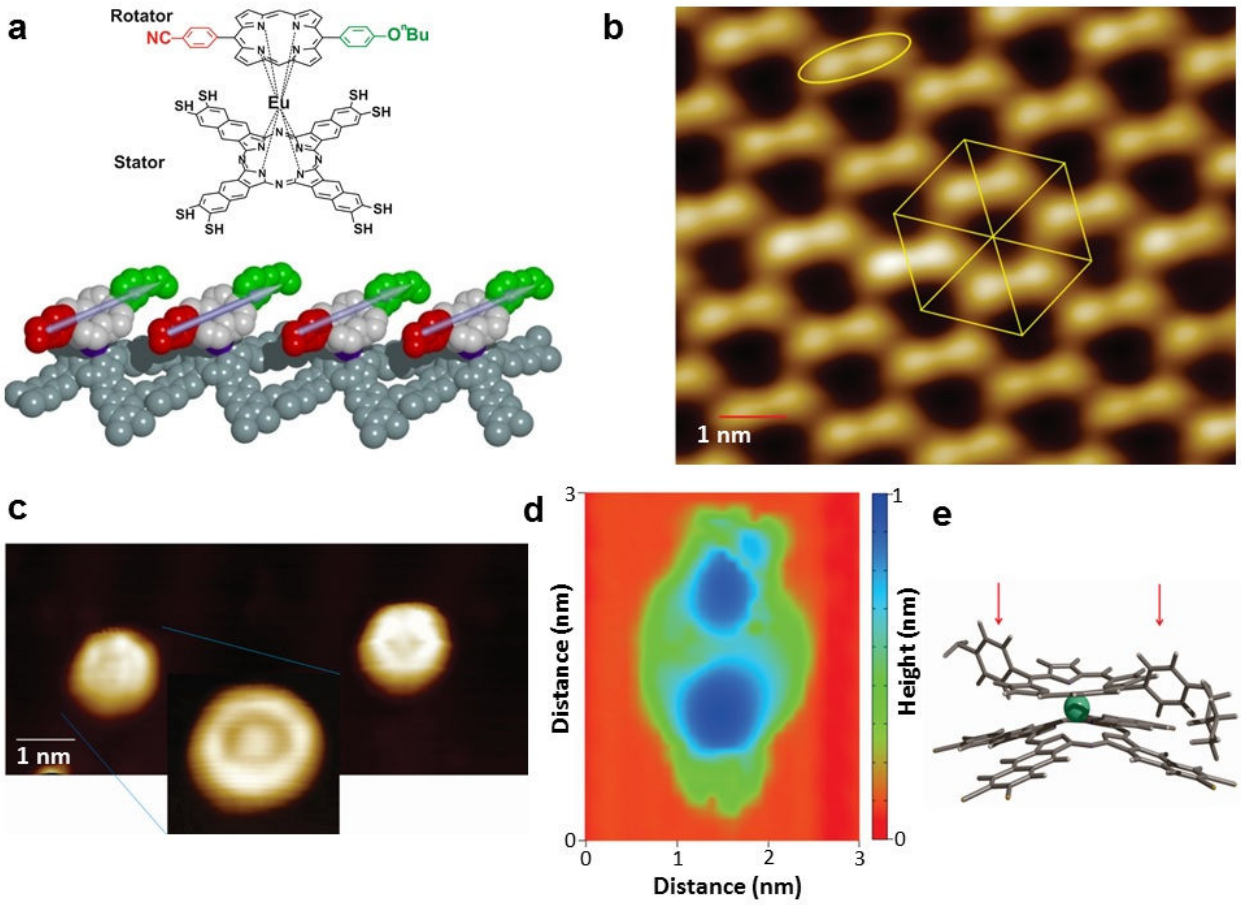
a
Rotator
NC
O^{n}Bu
Eu
SH
Stator
b
1 nm
c
1 nm
d
Distance (nm)
Distance (nm)
Height (nm)
0
1
2
3
e

Figure 1

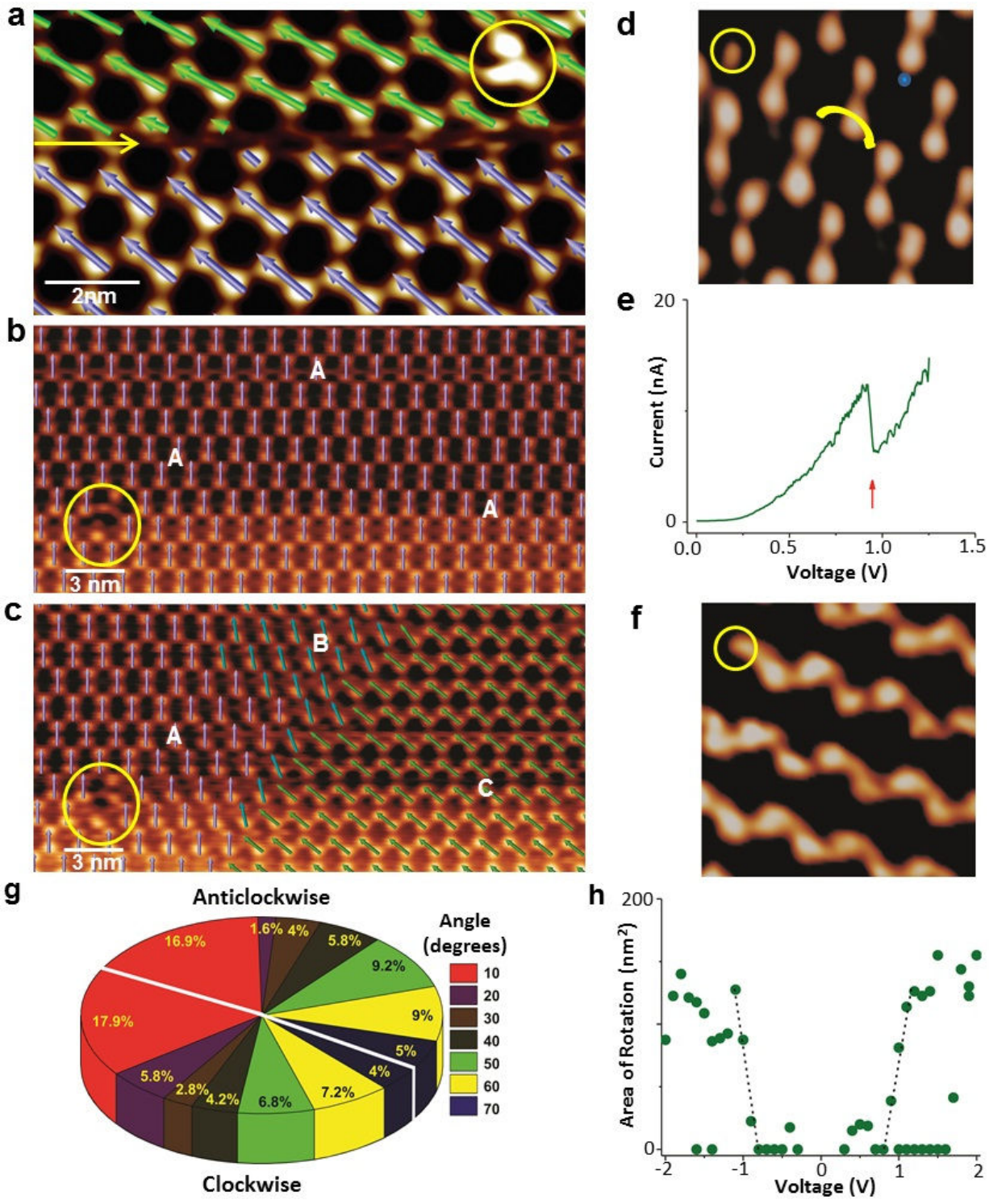
a
2nm
b
A
A
A
3 nm
c
B
A
C
3 nm
d
e
20
Current (nA)
0
0.0
0.5
1.0
1.5
Voltage (V)
f
g
Anticlockwise
Angle (degrees)
16.9%
1.6%
4%
5.8%
9.2%
9%
5%
4%
7.2%
6.8%
4.2%
2.8%
5.8%
17.9%
10
20
30
40
50
60
70
Clockwise
h
200
Area of Rotation (nm²)
0
-2
-1
0
1
2
Voltage (V)

Figure 2

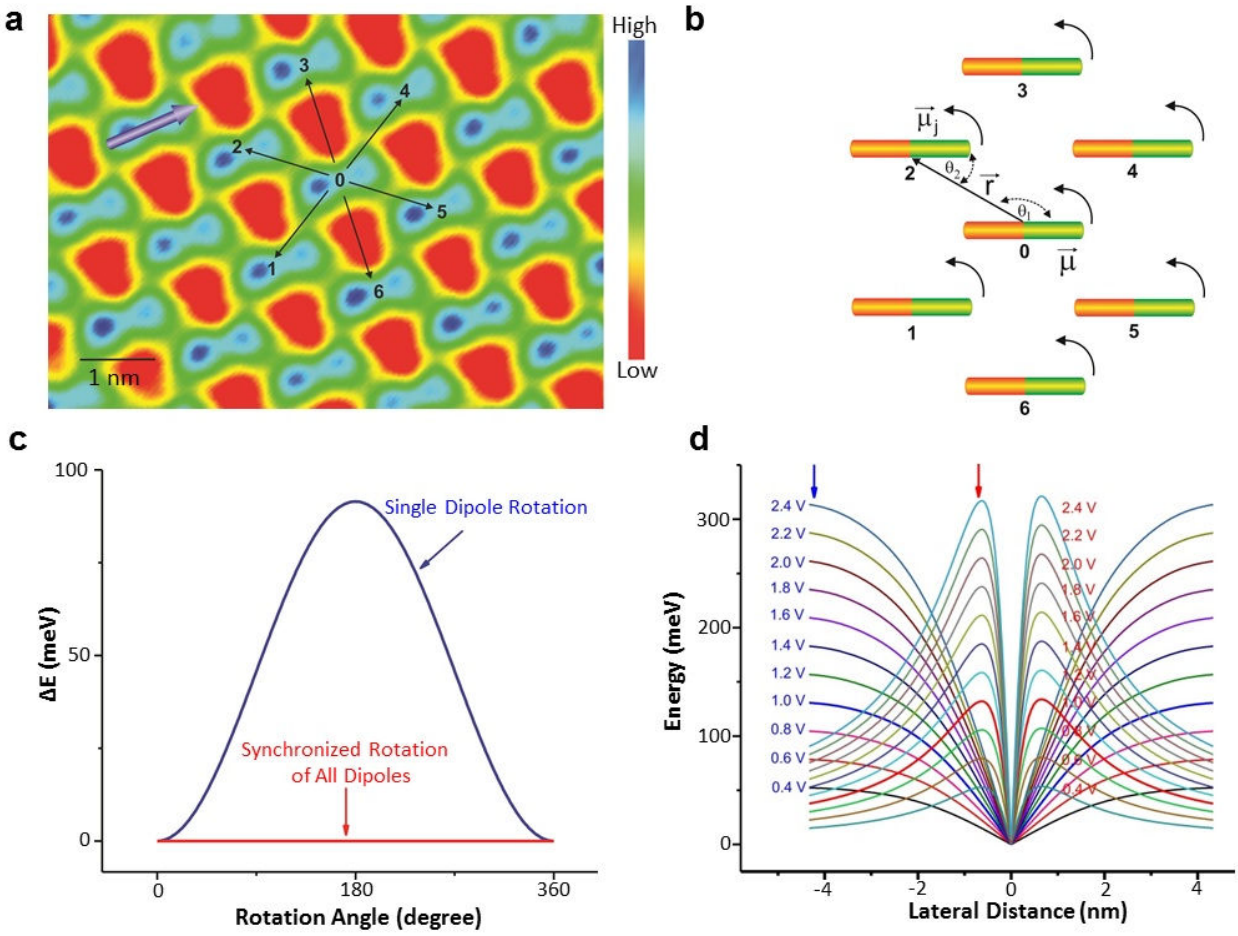
a
High
Low
1 nm
0
1
2
3
4
5
6
b
c
ΔE (meV)
100
50
0
Single Dipole Rotation
Synchronized Rotation
of All Dipoles
0
180
360
Rotation Angle (degree)
d
Energy (meV)
300
200
100
0
2.4 V
2.2 V
2.0 V
1.8 V
1.6 V
1.4 V
1.2 V
1.0 V
0.8 V
0.6 V
0.4 V
-4
-2
0
2
4
Lateral Distance (nm)

Figure 3

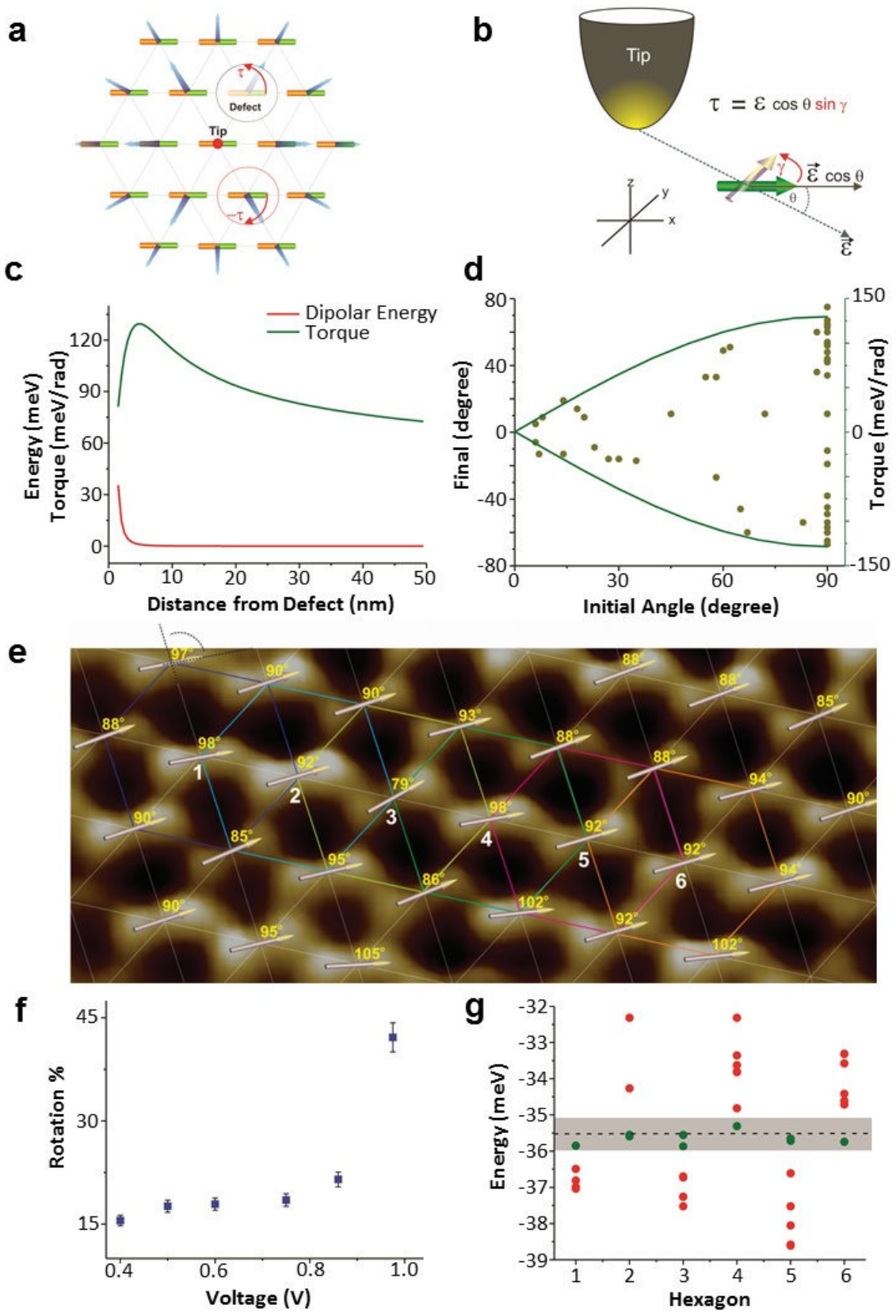
a
Defect
Tip
b
Tip
τ = ε cos θ sin γ
c
Dipolar Energy
Torque
Energy (meV)
Torque (meV/rad)
Distance from Defect (nm)
d
Final (degree)
Torque (meV/rad)
Initial Angle (degree)
e
f
Rotation %
Voltage (V)
g
Energy (meV)
Hexagon

Figure 4